Key Points:
- A statistical survey of satellite-derived signals of isolated convection initiation over central eastern China was conducted
- High signal frequency areas shift from northwest central eastern China in early summer to southeast central eastern China in midsummer
- The signals have longer lead times for isolated storm initiation in the late morning and afternoon, in early summer, and over highlands

Correspondence to:
W. Li,
lwb@pku.edu.cn

Distribution and Variability of Satellite-Derived Signals of Isolated Convection Initiation Events Over Central Eastern China

Yipeng Huang[1] iD, **Zhiyong Meng[1]**, **Jing Li[1]** iD, **Wanbiao Li[1]** iD, **Lanqiang Bai[1]** iD, **Murong Zhang[1]**, and **Xi Wang[2]**

[1]Laboratory for Climate and Ocean-Atmosphere Studies, Department of Atmospheric and Oceanic Sciences, School of Physics, Peking University, Beijing, China, [2]National Satellite Meteorological Center, China Meteorological Administration, Beijing, China

Abstract This study combined measurements from the Chinese operational geostationary satellite Fengyun-2E (FY-2E) and ground-based weather radars to conduct a statistical survey of isolated convection initiation (CI) over central eastern China (CEC). The convective environment in CEC is modulated by the complex topography and monsoon climate. From May to August 2010, a total of 1,630 isolated CI signals were derived from FY-2E using a semiautomated method. The formation of these satellite-derived CI signals peaks in the early afternoon and occurs with high frequency in areas with remarkable terrain inhomogeneity (e.g., mountain, water, and mountain-water areas). The high signal frequency areas shift from northwest CEC (dry, high altitude) in early summer to southeast CEC (humid, low altitude) in midsummer along with an increasing monthly mean frequency. The satellite-derived CI signals tend to have longer lead times (the time difference between satellite-derived signal formation and radar-based CI) in the late morning and afternoon than in the early morning and night. During the early morning and night, the distinction between cloud top signatures and background terrestrial radiation becomes less apparent, resulting in delayed identification of the signals and thus short and even negative lead times. A decline in the lead time is observed from May to August, likely due to the increasing cloud growth rate and warm-rain processes. Results show increasing lead times with increasing landscape elevation, likely due to more warm-rain processes over the coastal sea and plain, along with a decreasing cloud growth rate from hill and mountain to the plateau.

1. Introduction

Convection initiation (CI) is the process that leads to the initial formation of a convective storm (Ziegler, 2014). CI is the most crucial and challenging aspect in operational convection nowcasting (0–2 h forecasting) because of the complicated interaction between different scales and underlying surface conditions and the lack of intensive observations and thus complete understanding of boundaries and other processes that trigger convection. Considerable efforts have been made to examine CI-related processes in different regions, especially over America and Europe, as reviewed by Weckwerth and Parsons (2006). This present study explores the distribution and variability of satellite-derived signals of isolated CI events over central eastern China (CEC), a region with a typical monsoon climate.

An isolated CI event is the initiation of a newborn storm which is not attached to a preexisting storm. CI events embedded in or unseparated from other storms are generally excluded from satellite-based CI studies because of difficulties in collecting the satellite-derived signals. Examining the CI of isolated storms is important because isolated storms themselves can develop upscale into mesoscale convective systems (MCSs) (e.g., Houze et al., 2015; Houze et al., 2007; Rasmussen & Houze, 2016). Isolated storms can also affect the maintenance, organization, and development of preexisting storms, either by direct (e.g., merging) or by indirect (e.g., outflows) interaction, or both (e.g., Banta & Barker Schaaf, 1987; Purdom, 1976; Weaver & Nelson, 1982; Westcott, 1994). Isolated convection has also been shown to be key in the production of warm rain (Schumacher & Houze, 2003), greatly contributing to tropical and subtropical precipitation (e.g., Chen & Liu, 2016; Houze et al., 2015; Liu & Zipser, 2009; Qin & Fu, 2016). More importantly, forecasting an isolated CI event is quite difficult. Isolated convection is primarily driven by local, boundary layer processes (e.g., topography-induced circulations, drylines, sea breeze fronts, and horizontal convective rolls (Weckwerth & Parsons, 2006)) within a broad region of instability without significant large-scale forcing (Madaus &

Hakim, 2016; Markowski & Richardson, 2010). Local boundary layer processes are not well observed in the conventional observational network and are constantly affected by solar heating, topography, and environmental moisture and instability.

Geostationary satellite observations, which provide cloud top information at frequent intervals (<1 h), have been used as an important data source in CI research, because they can reveal early-stage cloud behaviors before precipitation is captured by radars, and thus may provide additional lead time for CI nowcasting. Purdom (1976) pioneered the usage of high-resolution visible (VIS) imagery from the Geostationary Operational Environmental Satellite (GOES) to reveal terrain- and thunderstorm-induced convective cloud lines leading to local storm initiation or intensification. Since then, VIS images have been utilized to show unique cloud behaviors before storm initiation in specific regions, such as the Colorado Rocky Mountains (Banta & Barker Schaaf, 1987; Barker Schaaf et al., 1988) and the southwest Amazon (Lima & Wilson, 2008). Furthermore, Roberts and Rutledge (2003) utilized 10.8 μm infrared (IR) brightness temperature (BT) to quantitatively examine vigorous cloud development ~30 min before the appearance of significant radar echoes.

With the enhancement of geostationary satellite capability, multispectral measurements, such as BT differences (BTDs) and their time trends, show great promise in providing precursor information for CI occurrence (Mecikalski et al., 2008, 2010a, 2010b, 2015; Mecikalski & Bedka, 2006; Siewert et al., 2010). The IR single and multispectral methods laid the foundation for the development of two satellite-based CI-nowcasting algorithms in the United States: the University of Wisconsin Convective Initiation (UWCI) nowcasting algorithm (Sieglaff et al., 2011) and the Satellite Convection Analysis and Tracking System (SATCAST) (Walker et al., 2012), respectively. These nowcasting efforts demonstrated that satellite-based nowcasts could provide different lead times for CI occurring in different convective environments. For example, based on SATCASTv2 (version 2), Walker et al. (2012) found a maximum difference of about 9 min in mean lead time between two unique convective regimes in the continental United States. However, the relationship between the lead times and satellite-derived cloud behaviors in different convective environments has been insufficiently documented. Mecikalski et al. (2013) made a regional comparison of GOES-derived cloud top properties before lightning initiation between Florida and Oklahoma. They found that Florida storms, which grew more slowly in a moister environment, showed longer lead times for lightning initiation predictions compared with Oklahoma storms, which grew explosively in a drier environment. Considering that only storm cases in two regions were analyzed in their study, a long-term and widespread statistical survey is needed to cover CI processes within more universal (diurnal, intraseasonal, and landscape) convective scenarios, to obtain a general picture of the possible variability in satellite-derived CI signals and thus a better understanding of CI processes, which will aid in issuing CI nowcasts.

CEC has an ideal climate regime for studying the climatology of convective storm initiation. During the warm season, the northward movement of the East Asia summer monsoon transports substantial warm and moist air from the tropics and subtropics into CEC with complex topography, resulting in diverse convective environments in this region (Luo et al., 2013; Xu, 2013). Being one of the most densely populated regions in the world (Small, 2004), CEC is vulnerable to storm-induced weather disasters. Recent efforts have strived to examine the general features of certain convective storms (e.g., developing cumulus congestus, squall lines, and MCSs) in CEC based on radar mosaics (e.g., Meng et al., 2013; Zheng et al., 2013) and satellite images (e.g., Ai et al., 2016; Wu et al., 2016; Yang et al., 2015). Most of these statistical studies have focused on the mature stages of convective clouds selected using some rigid criteria, for instance, cloud top BT $\leq -20°C$ in Wu et al. (2016) and radar reflectivity ≥ 40 dBZ in Meng et al. (2013). Using observations from the Tropical Rainfall Measuring Mission (TRMM) satellite, many studies have provided insights into convection of various types (e.g., shallow and deep convection) and from early through mature stages across the globe including parts of CEC (e.g., Houze et al., 2015; Liu et al., 2008; Schumacher & Houze, 2003; Xu, 2013; Zipser et al., 2006). However, TRMM observations only provide snapshots widely separated in time and cannot monitor cumulus cloud evolution of a CI event as geostationary satellite observations do. To date, systematic geostationary satellite-based CI studies mainly rely on observations from GOES for North and South America and the Meteosat Second Generation (MSG) for Europe. Here observations from Fengyun-2 (FY-2), the Chinese operational geostationary satellite, are utilized to glean a specific understanding of isolated CI characteristics in CEC.
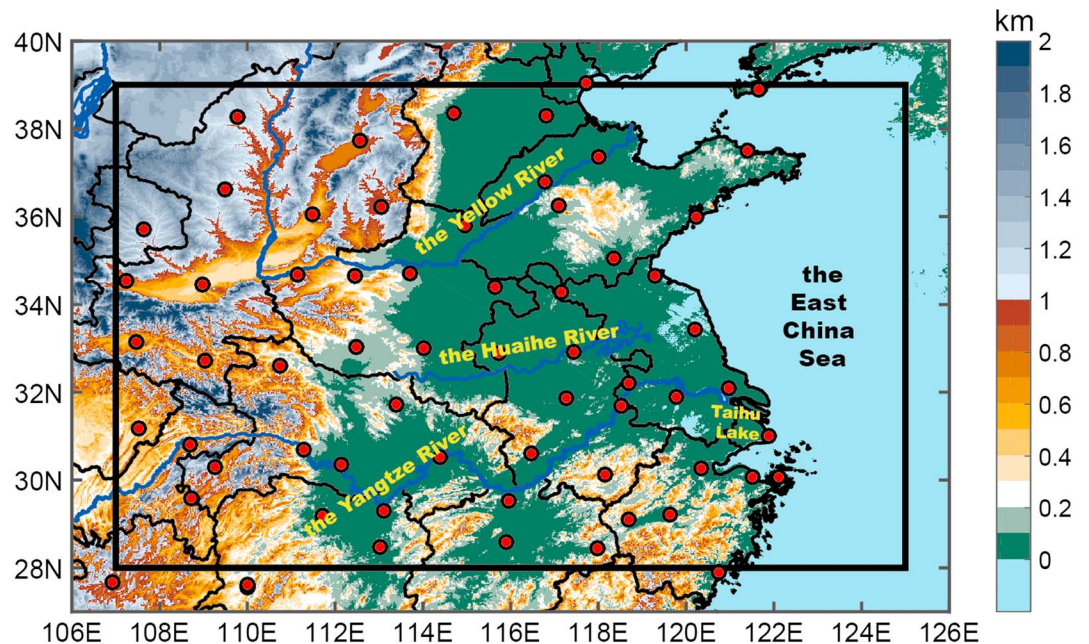
Figure 1. Topography map of central eastern China (solid box) and its vicinity, with the locations of operational radar stations used in this study (red dots). The province boundaries are marked by black lines. Important lake and river (blue lines) are labeled in yellow.

This present study intends to document the distribution and variability patterns of satellite-derived signals of isolated CI throughout the warm season of 2010 in CEC, including the location, formation time, cloud morphology, multispectral information, and lead time relative to the radar-derived CI signature. Each satellite-derived CI signal is checked against radar data to ensure that it represents the development of cumulus cloud undergoing isolated CI.

Section 2 introduces the data and methods used to identify the satellite-derived CI signals. Section 3 presents the spatial and temporal distributions of satellite-derived CI signals. The variability in the lead times of the signals is described in section 4. A summary is given in section 5.

2. Data and Methods

2.1. Satellite Data and Radar Mosaics

The satellite-derived signals of isolated CI from 23 April to 19 August 2010 (119 days in total) over CEC (28°–39°N, 107°–125°E, denoted by the solid box in Figure 1) were examined and validated based on data from FY-2E and radar mosaics, respectively.

FY-2E is China's third operational geostationary meteorological satellite for environmental monitoring and weather applications. Its data service is operated by the National Satellite Meteorological Center (NSMC) of the China Meteorological Administration (CMA). Launched on 23 December 2008, FY-2E was positioned above the equator at 104.5°E to extend the service of FY-2C up until 1 July 2015, after which it was repositioned at 86.5°E to extend the service of FY-2D. The Stretched Visible and Infrared Spin Scan Radiometer (S-VISSR) on board FY-2E has five broadband channels, including one VIS channel and four IR channels (IR1, IR2, IR3, and IR4), with 1.25 km and 5 km resolutions at nadir, respectively (Table 1). The IR and VIS images were respectively interpolated into 0.05° and 0.0125° grids of longitude and latitude in this study. During the study period, data from the five channels were collected every 30 min rather than 60 min as was used for the rest of the year. The satellite data are available at 99.5% of whole times during the study period. The 30 min interval data set available from FY-2E was utilized in this current study. Previous studies have demonstrated that satellite-derived 30 min interval fields can be used in inferring the physical attributes of growing cumulus clouds (e.g., Mecikalski et al., 2010a, 2010b; Siewert et al., 2010).

Table 1
Specification of S-VISSR On Board FY-2E

Channel name	Spectral range (μm)	Spatial resolution (km)
IR1	10.3–11.3	5
IR2	11.5–12.5	5
IR3	6.3–7.6	5
IR4	3.5–4.0	5
VIS	0.55–0.90	1.25

Digital mosaics of composite radar reflectivity (the horizontal distribution of vertical maximum radar reflectivity) are operationally provided by the National Meteorological Center of the CMA based on a network of Chinese Doppler weather radars (their locations are marked by red dots in Figure 1). With a 2 km × 2 km horizontal resolution and a time interval of 10 min, the radar mosaics covered 112 out of the 119 days during the study period. To match the radar and satellite data in time, the radar mosaics used in this study were examined every 30 min at the same times as those of the FY-2E data (i.e., 0000 UTC, 0030 UTC, 0100 UTC, etc.).

2.2. Identification of Isolated Convection Initiation From Radar Mosaics

An isolated storm is declared when a newborn storm cell, without a nearby (within 10 km in this study) preexisting storm or storm anvil (≥10 dBZ), reaches 35 dBZ and lasts over 30 min, and its CI time is defined as the first appearance of ≥35 dBZ radar reflectivity. The 35 dBZ criterion has been widely used in previous
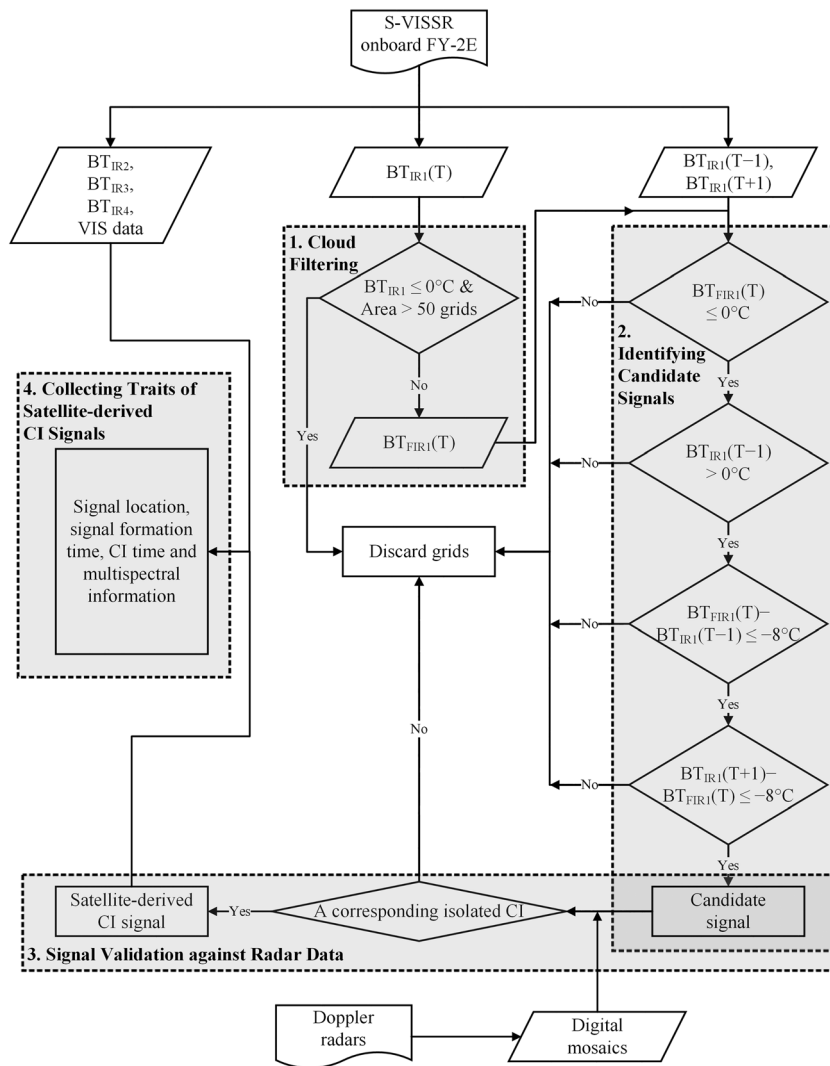

Figure 2. Flow chart of the semiautomated method used to identify the satellite-derived signals of isolated CI in this study. Instrument (rectangles with a wave-like base), data (parallelograms), process (solid rectangles), decision (diamonds), and main step (dashed boxes with gray shading) are presented.

studies to define CI (e.g., Mecikalski et al., 2015; Mecikalski & Bedka, 2006; Roberts & Rutledge, 2003; Senf & Deneke, 2017; Walker et al., 2012).

2.3. Identification of Satellite-Derived Signals of Isolated Convection Initiation

A semiautomated method was designed to identify satellite-derived CI signals over areas where there is persistent cloud growth that leads to isolated storm initiation. The production of candidate signals was solely based on the IR1 channel from FY-2E. IR1 has a central wavelength of 10.8 μm, which is a primary channel that provides cloud information, and has been widely used in previous CI studies. Once a candidate CI signal was verified by radar mosaics, its several traits were further collected. This method is detailed in the following four steps and illustrated in Figure 2.

1. *Cloud filtering*. A cloud filtering procedure was performed before searching the candidate signals for isolated CI at a given scan time T. Cumulus clouds undergoing isolated CI are always characterized as small newborn cloud cells. Clouds with an extensive area of $BT_{IR1} \leq 0°C$ are usually clouds that have evolved into a certain stage rather than immature cumulus clouds during the CI period. Thus, regions with a contiguous $BT_{IR1} \leq 0°C$ area larger than 50 grids ($>1,000$ km^2) were removed from the IR1 image. The filtered BT_{IR1} is named BT_{FIR1} in Figure 2.

2. *Identifying candidate signals*. BT_{FIR1}, the filtered BT_{IR1} from step 1, was then used to produce candidate signals through four procedures. The vigorous cloud growth leading to CI can be characterized from satellite observations by IR1 signatures with subfreezing cloud top BTs and significant cooling rates (Roberts & Rutledge, 2003). To search the signals at time T, three consecutive times of IR1 data were required, including BT_{IR1} at the previous scan ($BT_{IR1}(T-1)$), BT_{FIR1} at the current scan ($BT_{FIR1}(T)$), and BT_{IR1} at the next scan ($BT_{IR1}(T+1)$).

   The first procedure is to identify the occurrence of a subfreezing cloud top at the current scan T (i.e., $BT_{FIR1}(T) \leq 0°C$ in Figure 2). The second procedure is to ensure that the cumulus cloud identified at T evolves from a warm cloud or a cloudless condition at the previous scan (i.e., $BT_{IR1}(T-1) > 0°C$ in Figure 2). The first two procedures are similar to a CI indicator in describing cumulus cloud top glaciation in previous studies (Mecikalski et al., 2008, 2010a; Mecikalski & Bedka, 2006; Siewert et al., 2010). The next two procedures are to ensure persistent growth of the cumulus clouds from $T-1$ to $T+1$. The cooling rate was calculated as the difference between $BT_{IR1}(T-1)$ and $BT_{FIR1}(T)$ for each grid in the third procedure. Only the grids with a cooling rate of $\geq 8°C$ $(30$ min$)^{-1}$ were kept for further processing (i.e., $BT_{FIR1}(T) - BT_{IR1}(T-1) \leq -8°C$ in Figure 2). Within our 30 min interval framework, the 8°C $(30$ min$)^{-1}$ criterion was chosen based on previous studies (e.g., Mecikalski & Bedka, 2006; Siewert et al., 2010). For example, these studies used the criteria of a $\geq 4°C$ $(15$ min$)^{-1}$ cooling rate combined with a sustained cooling rate for a 30 min period in CI nowcasting applications. The last procedure is similar to the third, except for requiring $BT_{IR1}(T+1) - BT_{FIR1}(T) \leq -8°C$ (Figure 2). Any grid at T that failed any one of the four procedures was discarded. Clusters of remaining grids that passed all the four procedures were identified as candidate signals of isolated CI for further validation.

3. *Signal validation against radar data*. The candidate signals generated from step 2 were manually checked in this step to ensure that there was a corresponding isolated CI event in the radar mosaics. A candidate signal was categorized as a "satellite-derived CI signal" when the signal-related cloud overlapped a radar-observed isolated storm at CI time. Otherwise, it was discarded as a "false signal". Only the satellite-derived CI signals after this step were used for further analysis. Figure 3 exemplifies some satellite-derived CI signals at different given scans (white polygons in Figures 3a2, 3b2, and 3c2) with corresponding radar echoes (black circles in Figures 3a4, 3b4, and 3c4).

4. *Collecting traits of satellite-derived CI signals*. Several traits of the satellite-derived CI signals were derived from the IR data and radar mosaics. These traits include the following: (1) signal location, (2) signal formation time (the aforementioned scan time T), (3) CI time (the occurrence time of isolated CI in radar observations corresponding to a satellite-derived CI signal), and (4) multispectral information.

   To obtain multispectral information for each satellite-derived CI signal, other IR channel measurements from the S-VISSR were also used besides BT_{IR1}. Previous efforts have shown great promise in relating IR "interest fields" (a series of spectral and temporal differencing fields) to the physical attributes of developing cumulus clouds undergoing CI (e.g., Mecikalski et al., 2010a, 2013, 2015; Mecikalski & Bedka,
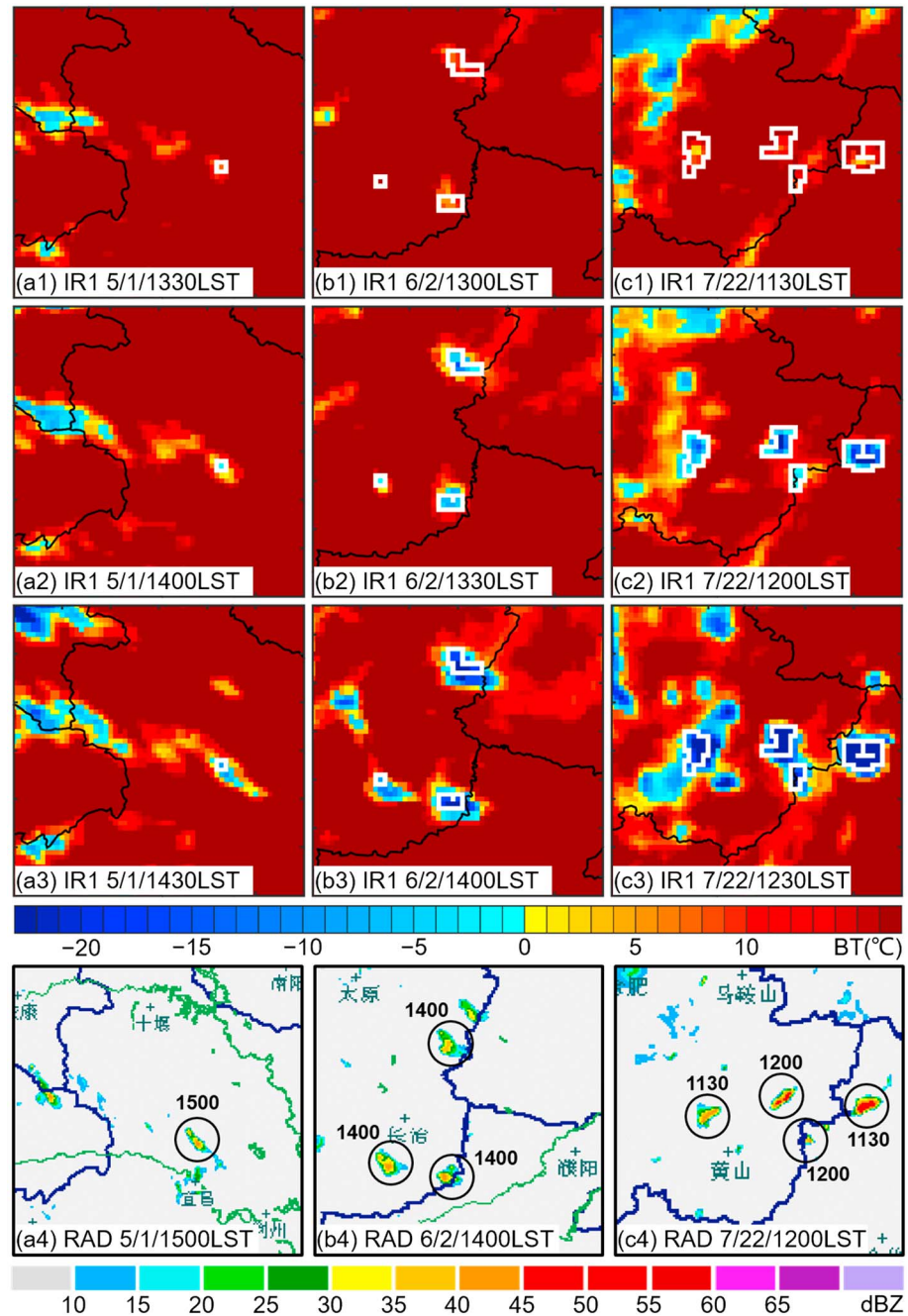
Figure 3. Typical examples of satellite-derived signals of isolated CI over central eastern China for (a1–a4) May, (b1–b4) June, and (c1–c4) July and August. Each column presents at least one signal (white polygon) identified by the semiauto-mated method illustrated in Figure 2. Signals in the same column indicate that they have the same formation time. For each signal, three successive IR1 images at $T-1$ (Figures 3a1, 3b1, and 3c1), T (Figures 3a2, 3b2, and 3c2), and $T+1$ (Figures 3a3, 3b3, and 3c3) are given. Radar signatures corresponding to the satellite-derived CI signals are denoted by the black circles in radar (RAD) mosaics (Figures 3a4, 3b4, and 3c4). The label near the circle represents the CI time for the corresponding isolated storm, i.e., the first occurrence time of $\geq$35 dBZ reflectivity in the isolated storm.

2006; Senf & Deneke, 2017; Siewert et al., 2010). Since the S-VISSR has four IR channels (Table 1), the available interest fields from FY-2E include BT_{IR1}, $BTD_{IR2-IR1}$, $BTD_{IR3-IR1}$, $BTD_{IR3-IR2}$, $BTD_{IR4-IR1}$, and their respective time trends. Each interest field can be used to describe at least one cloud top characteristic as summarized in Table 2. Once a satellite-derived CI signal was identified, interest fields associated with this signal were collected.

Table 2
The Interest Fields Available From FY-2E for Assessing the CI-Related Cloud Top Characteristics and Their GOES/MSG Counterparts, Physical Description, Critical Values in Previous Studies, and Mean Value (Standard Deviation) in This Study

FY-2E interest field	GOES/MSG counterpart	Physical description	Critical value in previous studies	Mean value (standard deviation) in this study
BT_{IR1}	10.8 μm BT	Cloud top height/glaciation	<0°C (Mecikalski & Bedka, 2006)$_1$	−5.0°C (3.67°C)
BT_{IR1} 30 min trend	10.8 μm BT 30 min trend	Cloud growth rate (vertical)	<15 min trend <−4°C (15 min)$^{-1}$ (Mecikalski & Bedka, 2006)	−17.3°C (6.11°C)
$BTD_{IR2-IR1}$	12.0−10.8 μm BTD	Cloud top height	−3 to 0°C (Mecikalski & Bedka, 2006)	0.35°C (1.19°C)
$BTD_{IR2-IR1}$ 30 min trend	12.0−10.8 μm BTD 30 min trend	Cloud growth	>0°C (Siewert et al., 2010)	1.53°C(0.98°C)
$BTD_{IR3-IR1}$	6.5 (6.7)−10.8 μm BTD	Cloud top height relative to middle/upper troposphere	−35 to −10°C (Mecikalski & Bedka, 2006)	−24.8°C (3.08°C)
$BTD_{IR3-IR1}$ 30 min trend	6.5 (6.7)−10.8 μm BTD 30 min trend	Cloud growth toward middle/upper troposphere	>6°C (Mecikalski & Bedka, 2006)[a]	12.0°C (4.01°C)
$BTD_{IR3-IR2}$	6.5 (6.7)−12.0 μm BTD	Cloud top height relative to middle/upper troposphere	Unknown	−25.2°C (2.68°C)
$BTD_{IR3-IR2}$ 30 min trend	6.5 (6.7)−12.0 μm BTD 30 min trend	Cloud growth toward middle/upper troposphere	Unknown	10.5°C (3.56°C)
$BTD_{IR4-IR1}$	3.9−10.8 μm BTD	Cloud top glaciation	>17°C (Harris et al., 2010)	23.9°C (8.12°C)
$BTD_{IR4-IR1}$ 30 min trend	3.9−10.8 μm BTD 30 min trend	Cloud top glaciation	>3°C (Harris et al., 2010)[a]	9.0°C (5.80°C)

[a]Values are doubled from 15 min trend, as shown in relevant previous studies.

Statistical analyses on the 10 FY-2E interest fields of all satellite-derived CI signals at *T* were compared with typical values of the GOES/MSG interest fields for cumulus clouds undergoing CI from previous research (Table 2). The values of most FY-2E fields agree well with their GOES/MSG counterparts, indicating that the satellite-derived CI signals in our study can be used to represent cloud properties undergoing CI. Similar to Wu et al. (2016), the $BTD_{IR2-IR1}$ field, in which a higher value represents a higher cloud top and the magnitude is influenced by moisture (especially low-level and cloud top moisture), shows a positive bias relative to the reference value. This positive bias was attributed by Wu et al. (2016) to the larger >12.0 μm spectral portion (more sensitive to moisture) of the IR2 spectral response function of FY-2E compared with its counterparts from other satellites including GOES and MSG, and the radiation emitted by the warm moisture brought from lower levels by strong updrafts, both of which resulted in larger BT_{IR2} and thus larger $BTD_{IR2-IR1}$. No reference $BTD_{IR3-IR2}$ and its time trend were available. However, Mecikalski et al. (2010a) showed that the $BTD_{IR3-IR1}$ and its time trend could be used as substitutes for $BTD_{IR3-IR2}$ and its time trend to describe cloud top height relative to middle/upper troposphere and cloud growth toward middle/upper troposphere, respectively. Such substitutability was also verified by the significantly high correlations ($r > 0.9$) between $BTD_{IR3-IR1}$ and $BTD_{IR3-IR2}$ and also between their 30 min trends in our study.

In addition, the elevations at all signal locations were estimated using the 1 arc min gridded elevations and bathymetry for the world (ETOPO1) (Amante & Eakins, 2009). The cloud morphology corresponding to daytime signals was also investigated based on high-resolution VIS images.

2.4. The Representativeness of Satellite-Derived CI Signals

The representativeness of the satellite-derived CI signals identified in this study was examined using the probability of detection (POD). The POD is the ratio of the number of satellite-derived CI signals to the number of radar-detected isolated CI events in the same category. During the study period, a total of 3,239 isolated CI events were identified from radar mosaics, and the total number of satellite-derived CI signals is 1,630. The POD for the entire CEC is 50.3%. This POD value is comparable with the results of Sieglaff et al. (2011). They obtained 56.3% and 47.0% PODs of CI events in a severe storm risk area and the Central United States, respectively, based on a 15 min IR-only method.

Some main sources of error can negatively affect the POD. First, low-level CI-related cumulus clouds sometimes are obscured by higher-level cirrus clouds or cloud anvils in IR images, such that the cumulus cloud top BTs cannot be accurately measured by the satellite (e.g., Mecikalski et al., 2010a; Sieglaff et al., 2011). Second, the 30 min FY-2E data may be of too low temporal resolution to monitor some CI processes. A third main source of error is the likelihood that some subgrid cloud growth leading to CI process may not be well
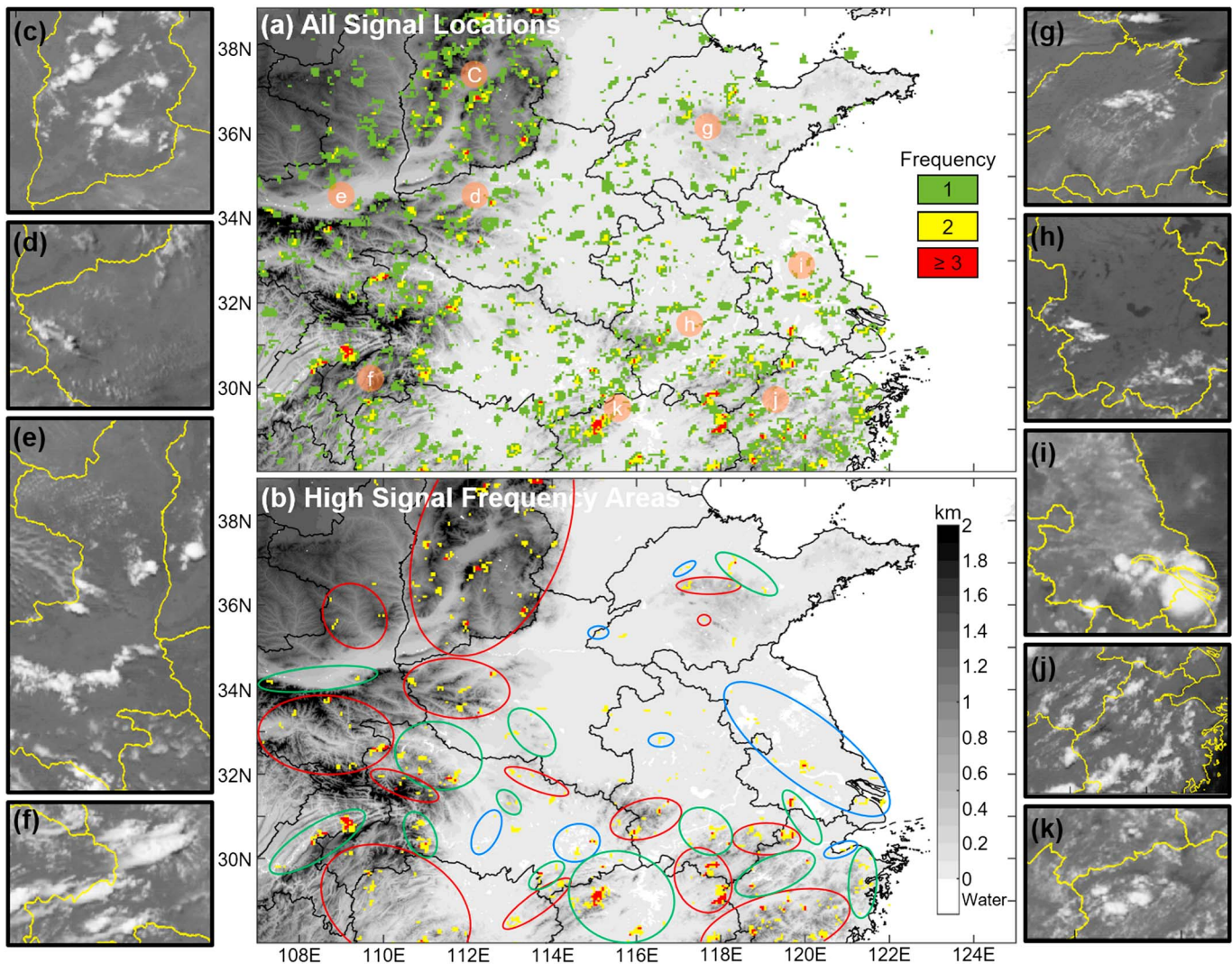
Figure 4. Geographical distributions of (a) all satellite-derived CI signal locations and (b) high signal frequency areas over central eastern China from 23 April to 19 August 2010. High signal frequency areas are defined as the grids where signals occur repeatedly (frequency > 1). The gray shading in Figures 4a and 4b denotes the terrain height. Four types of high signal frequency areas are presented in Figures 4b: mountain areas (red circles), water areas (blue circles), mountain-water areas (green circles), and other areas (remaining areas without markers). (c–k) Typical examples of the morphology of cumulus clouds undergoing CI over high signal frequency areas in VIS images to demonstrate their collocations with corresponding topography denoted by corresponding letters c–k in Figure 4a.

captured by the satellite due to the limited spatial resolution (Walker et al., 2012). In fact, these sources of error are quite common in satellite-based CI research.

3. Spatial and Temporal Distributions of Satellite-Derived CI Signals

3.1. Spatial Distribution

A total of 1,630 satellite-derived signals in CEC were identified to have a corresponding radar-based isolated CI event from 23 April to 19 August 2010. Overall, the occurrence of these signals is widespread across CEC (Figure 4a). The POD variability is very small (within 4%) across different landscapes in CEC, suggesting the reliability of the spatial distribution of satellite-derived CI signals. However, when considering high signal frequency areas where satellite-derived CI signals repeatedly occur, their distribution shows clear terrain dependence (Figure 4b), reflecting the important role of local topography in isolated CI (e.g., Houze, Wilton, & Smull, 2007; Medina et al., 2010; Rasmussen & Houze, 2011, 2016). Some examples of the collocations between terrain features and CI-related cloud morphology in VIS images are given in Figures 4c–4k. High signal frequency areas (Figure 4b) can be geographically classified into four categories:
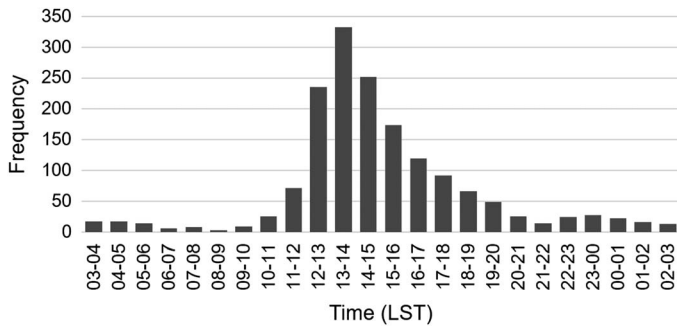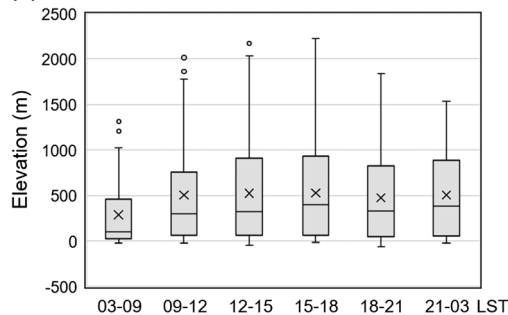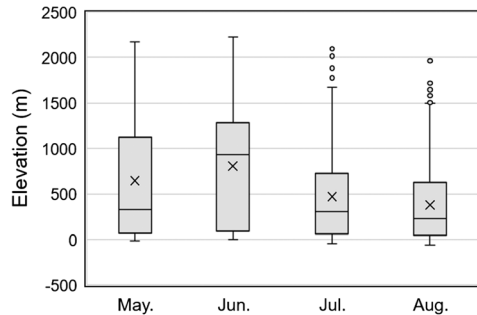
Figure 5. Diurnal distribution of signal formation frequency (in LST, LST = UTC +8 h).
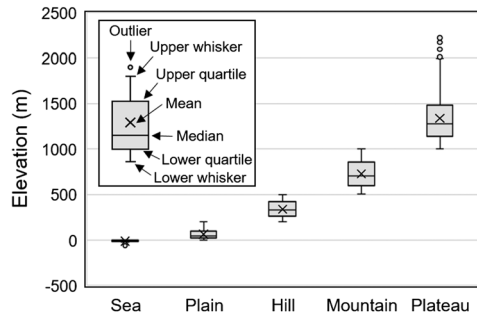

Figure 6. Box-and-whisker plots of the (a) diurnal, (b) monthly, and (c) landscape distributions of signal location elevations. The plotting style for all box-and-whisker plots in this study is exemplified in Figure 6c. The whole day is divided into six 3 h or 6 h periods in Figure 6a to ensure the sample size for each period and thus statistical significance. Five landscapes in Figure 6c are selected according to elevation range: coastal sea (<0 m), plain (0–200 m), hill (200–500 m), mountain (500–1000 m), and plateau (>1000 m).

1. *Mountain areas*. Typical mountain areas (highlighted by red circles in Figure 4b) cover the plateaus, mountains, and hills in the northwest, southwest, and southeast CEC, respectively. In these areas, there are remarkable elevation gradients due to the steep mountain slopes and especially the isolated mountain ridges (e.g., Figures 4c, 4d, 4g, and 4h). High signal frequency areas in this category are similar to "genesis zones" in the Colorado Rocky Mountains of the western United States where mountain thunderstorms commonly originate (Banta & Barker Schaaf, 1987; Barker Schaaf, Wurman, & Banta, 1988). Numerous efforts have demonstrated the important role of mountains in triggering and intensifying convection by both mechanical lifting and thermal heating (e.g., Houze, 2012; Soderholm et al., 2014; Wulfmeyer et al., 2008).

2. *Water areas*. This category (denoted by blue circles in Figure 4b) covers the coastlands, the Yangtze, Huaihe, Yellow River basins (refer to their locations in Figure 1), and the large lake basins in CEC. As a result of differential heating between water bodies (i.e., seas, rivers, and lakes) and their vicinal flatlands, sea, river, and lake breeze fronts usually form and move inland. These breeze fronts may enhance the convergence over the flatlands and aid in convection development, which is more apparent when synoptic-scale forcing is weak (e.g., Fovell, 2005; Laird et al., 2001; Purdom, 1976). A representative water area is the Yangtze River Delta (Figure 4i), which is adjacent to Taihu Lake and the East China Sea.

3. *Mountain-water areas*. Mountain areas surrounded by considerable water areas are classified into this category (highlighted by green circles in Figure 4b). Enhancements of convection and precipitation by the combined effects of orography (e.g., forced lifting) and its surrounding water bodies (e.g., moisture source) have been well studied (e.g., Qian et al., 2012; Umek & Gohm, 2016). Most of the high signal frequency areas in this category are located in the mountain areas along the Yangtze River, the Yellow River, and the coastlines, as well as in the mountain areas with adjacent large lakes (e.g., Figures 4e, 4f, 4j, and 4k).

4. *Other areas*. This category includes the areas that do not belong to any of the above three categories. These areas may feature other land surface inhomogeneity as a result of different land cover types, such as urban areas versus suburb areas, forests versus croplands, and wet areas versus dry areas (Gambill & Mecikalski, 2011; Weaver & Avissar, 2001).

3.2. Diurnal Distribution

Approximately half of the satellite-derived CI signals were identified in the early afternoon, peaking at 1200–1500 local standard time (LST = UTC + 8 h) (Figure 5). This distribution reconfirms the dominant impact of solar heating on isolated storm initiation (Markowski & Richardson, 2010). The POD of the satellite-derived CI signals also shows a diurnal variability within 19% (with a maximum POD of 58.4% at 1200–1500 LST and a minimum POD of 39.8% at 2100–0300 LST), which is larger than that 4% over different landscapes. However, this amplitude is much smaller than that of the diurnal variability of CI signals, indicating the reliability of the diurnal distribution of satellite-derived CI signals.

Overall, the satellite-derived CI signals forming at 0300–0900 LST are located over lower elevation areas compared with those forming at other periods (Figure 6a), mainly over valleys, waters, and flats. The inversion of thermal circulation may account for this diurnal distribution. For example,
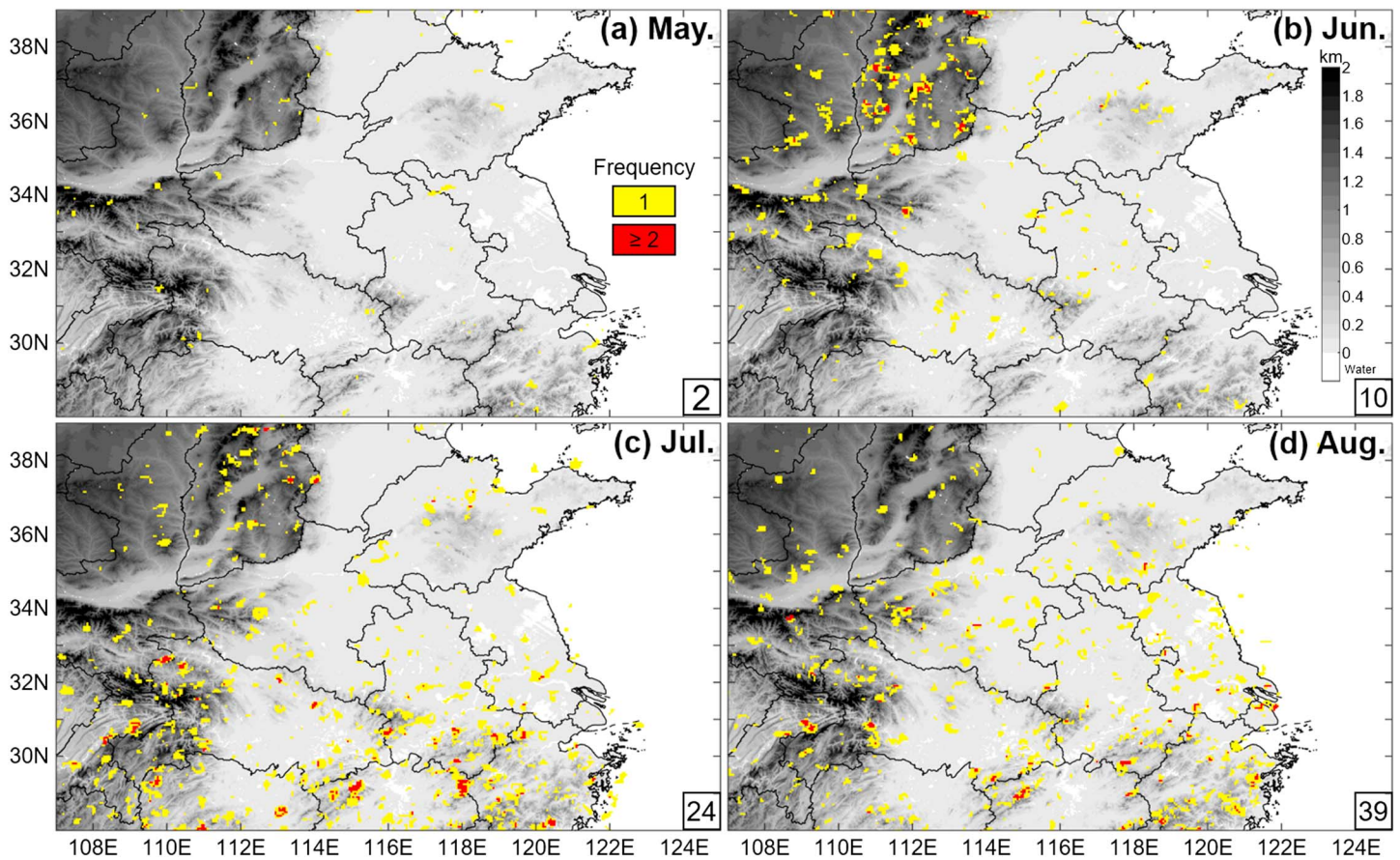
Figure 7. Geographical distributions of signal locations in (a) May (incorporating the April days), (b) June, (c) July, and (d) August during the study period. The gray shading denotes the terrain height. The monthly mean frequency of satellite-derived CI signal formation for each month is given in the lower right corner of each panel (unit: per day).

0300–0900 LST is the coldest period in a day (refer to BT_{IR1} at $T − 1$ in Figure 11), during which mountain breezes prevail (Yang & Slingo, 2001) and favor more convective activity occurring over lower elevation areas. After that, the signals consistently appear over higher-elevation areas, likely due to the prevailing valley breezes, especially during 1200–1800 LST (Figure 6a) when solar heating is strongest.

3.3. Intraseasonal Distribution

The satellite-derived CI signals apparently increase from early summer (i.e., May and June) to midsummer (i.e., July and August). The monthly mean frequency increases from 2 per day in May (incorporating the April days in the following analyses) to 39 per day in August (Figure 7). In May, the satellite-derived CI signals are sparse over CEC and mainly occur in the plateau mountains (Figure 7a). This preference is further confirmed in June, when more signals appear near the mountain ridges over plateau regions (Figure 7b). In July and August, the satellite-derived CI signals extensively outbreak over the whole of CEC, with a high frequency in the southeast part (Figures 7c and 7d). Results show that the POD varies very slightly between months (within 4.5%), indicating the reliability of the intraseasonal distribution of satellite-derived CI signals.

The intraseasonal distribution of satellite-derived CI signals is associated with the seasonal migration of the East Asia summer monsoon (EASM). During early summer, the EASM is active over south China (Luo et al., 2013). Both the moisture (Figure 8) and instability (Figure 9) are small in CEC. The lifting is generally localized rather than at larger scales. The more frequent satellite-derived CI signals in northwest CEC (Figures 7a and 7b) are likely attributed to the terrain forcing locally provided by the steep plateau mountains. As the EASM moves northward during midsummer, a moister environment (Figure 8) with increasing convective instability (Figure 9) may reduce the terrain-elevation demand as a thermal or mechanical lifting mechanism for isolated CI (Figure 6b) and contributes to the massive outbreak of satellite-derived CI signals
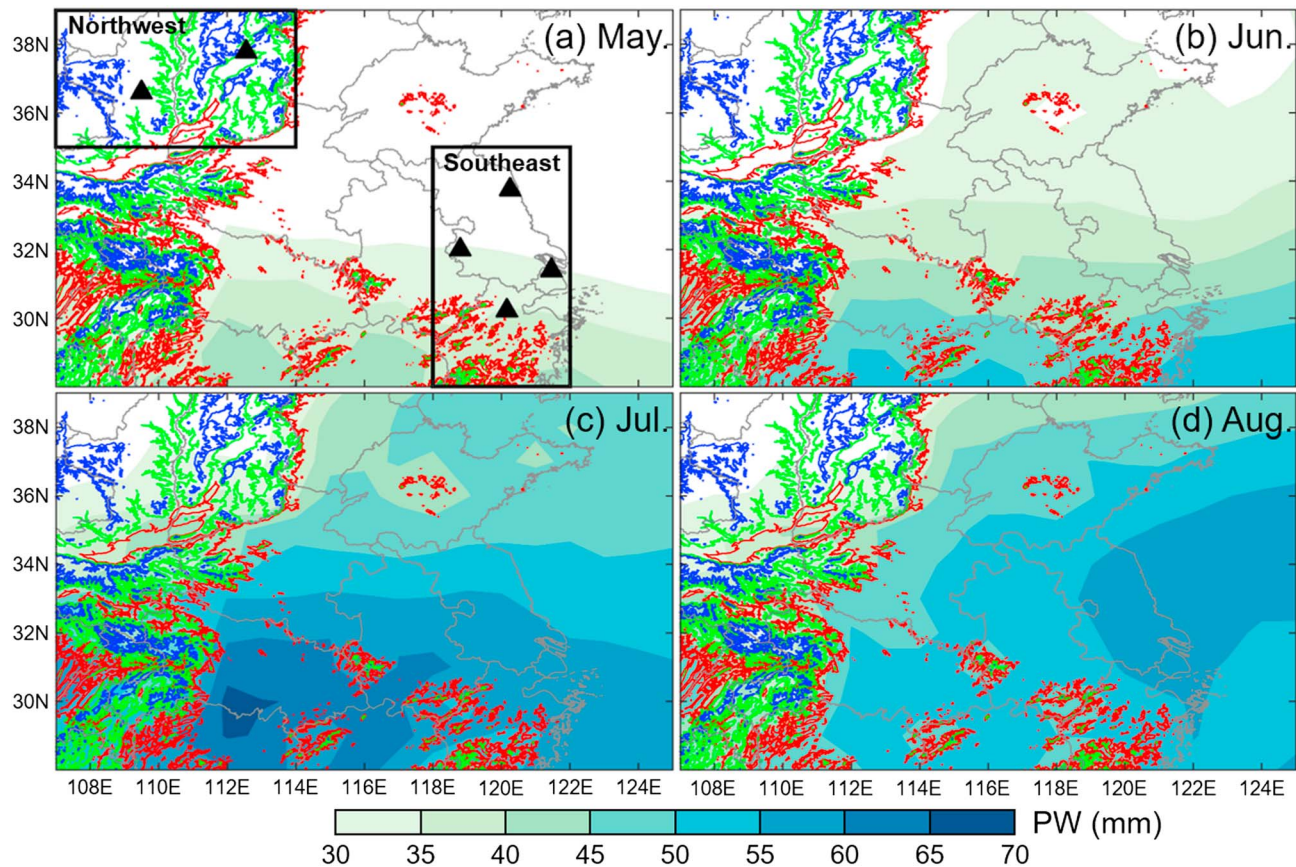
Figure 8. Monthly mean precipitable water (PW) in (a) May, (b) June, (c) July, and (d) August over central eastern China. Data are obtained from National Centers for Environmental Prediction Final Operational Global Analysis (NCEP FNL) with a horizontal resolution of 1° × 1° every 6 h from 1 May to 31 August 2010. The red, green, and blue contour lines represent the topographic elevation of 500, 1,000, and 1,500 m, respectively. The solid boxes in Figure 8a denote two distinct equal-area regions selected for further analysis in Figure 9: northwest (35°–39°N, 107°–114°E) and southeast (28°–35°N, 118°–122°E) regions. The black triangles represent the six rawinsonde stations within the northwest and southeast regions.

especially over southeast CEC (Figures 7c and 7d). The northward movement of the EASM also increases larger-scale lifting and thus leads to the northward shift of the high-frequency areas of organized convective systems (e.g., Luo et al., 2013; Meng et al., 2013; Yang et al., 2015). In midsummer, the less frequency of the satellite-derived CI signals over northwest CEC is likely due to the decrease of localized lifting, and less moisture and instability left with more frequent occurrence of organized systems in north CEC depriving the moisture and instability.

4. Lead Time of Satellite-Derived CI Signals Relative to Radar-Derived CI Signatures

The lead time of satellite-derived CI signals relative to radar-derived CI signatures is very important in CI nowcasting. The variability of the lead time of satellite-derived CI signals in different convective scenarios is examined in this section. The lead time (LT) of each satellite-derived CI signal was calculated as the difference between signal formation time and CI time. Within the 30 min interval framework in our study, LTs are integer multiples of 30 min, ranging from −30 to 120 min. Negative LTs represent situations when satellite-derived CI signal forms after the occurrence of radar-derived CI. Warm-rain processes in early stages of cloud development should largely account for negative LTs. Warm rain is defined as "rain formed from a cloud having temperatures at all levels above 0°C, and resulting from the droplet coalescence process" (American Meteorological Society, 2017). Given that the signal formation time is recognized only when the signal-related cloud top reaches subfreezing level (i.e., BT_{FIR1} at $T \le 0°C$, Figure 2), those CI cases where the cloud forms through a warm-rain process may have a negative or zero LT. Some examples of satellite-derived CI signals undergoing warm-rain process are given in Figures 3c1–3c4.
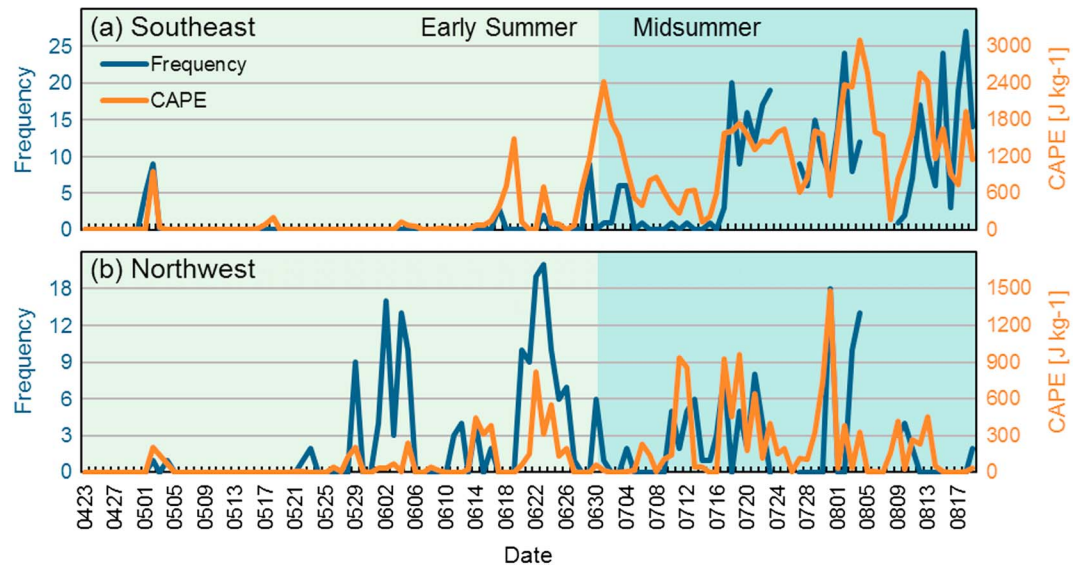
Figure 9. Daily variation of satellite-derived CI signal frequency (blue line) and the most unstable convective available potential energy (MUCAPE; orange line) from 23 April to 19 August 2010 for the (a) southeast and (b) northwest regions in central eastern China. The locations of these two regions are given in Figure 8a. The daily MUCAPE for each region was calculated as the mean value of MUCAPE from several soundings (their locations are given in Figure 8a) at 0000 UTC. The MUCAPE in an observed sounding was calculated with virtual temperature correction and within the lowest 300 hPa above the ground. The light and dark cyan shadings denote the periods of early summer and midsummer, respectively. Two breakages in the blue lines on 24–26 July and 5–8 August are due to the lack of radar mosaics to identify satellite-derived CI signal.

The LT variability is interpreted using IR1 fields which reflect the CI-related convective environment and cloud top characteristics detected by satellite. The variabilities of FY-2E interest fields are demonstrated in box-and-whisker plots as a function of scan time (before ($T-1$), at (T), and after ($T+1$) signal formation) or scan interval between $T-1$ and $T+1$.

4.1. Diurnal Variation

The LT of satellite-derived CI signals in the late morning and afternoon is overall longer than that in other periods (Figure 10a). The mean LT of signals at 0900–1800 LST is 9 min. After sunset, the LT begins to decline and even switches into a lag time at 0300–0900 LST with a mean value of −2 min.

The diurnal variation in LT is likely a result of different diurnal features of BT_{IR1} at $T-1$ and T. As mentioned in section 2, the identification of a satellite-derived CI signal requires a ≥8°C $(30\ \text{min})^{-1}$ cooling rate of BT_{IR1} between T and $T-1$ (Figure 2). At $T-1$ when cloud is not present yet or appears at low levels, the magnitude of BT_{IR1} greatly depends on terrestrial radiation, which is primarily modulated by solar heating. Therefore, stronger solar heating in the late morning and afternoon (0900–1800 LST) results in stronger terrestrial radiation and thus higher BT_{IR1} (Figure 11) in a day. During the late evening and early morning (2100–0900 LST) when solar heating is lacking, the terrestrial radiation is weaker and thus the BT_{IR1} is lower (Figure 11). On average, the magnitude of BT_{IR1} at $T-1$, ranging from 9°C (0300–0900 LST) to 13°C (1200–1500 LST), exhibits an apparent diurnal variation. However, at T when high cloud develops, the BT_{IR1} is mainly determined by cloud top radiation and does not have apparent diurnal variation (Figure 11; the diurnal bias in mean BT_{IR1} is about 1°C). Consequently, in the late evening and early morning, the lower BT_{IR1} at $T-1$ results in a weaker cooling signature in IR1 images between T and $T-1$, which is more difficult to meet the cooling rate threshold in detecting CI-related signals. This may lead to the short or even negative LTs during this period (Figure 10a).

4.2. Intraseasonal Variation

Overall, LT shows a monthly declining trend from May to August. The mean LT decreases from 35 min in May down to 1 min in August (Figure 10b). No negative LT appears in May (Figure 12a) and only a few in June
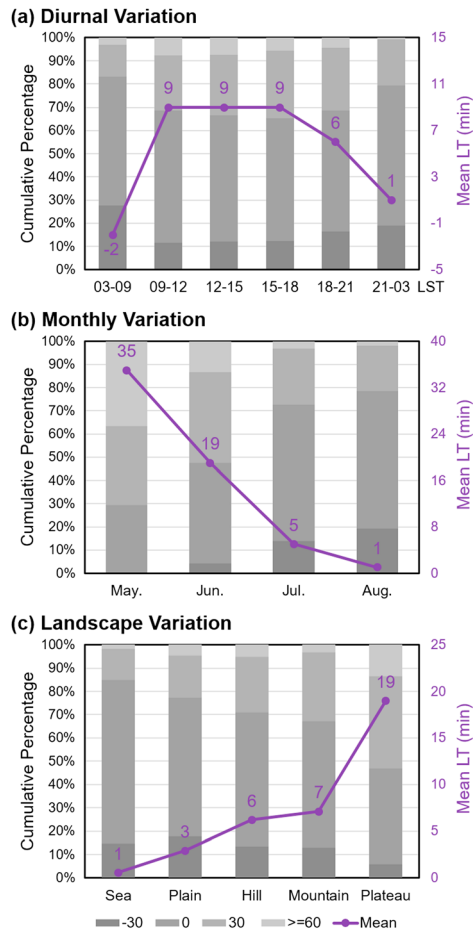
Figure 10. The (a) diurnal, (b) monthly, and (c) landscape variations of LT (the lead time of signal formation time before the CI time) distribution. Within the 30 min interval framework in this study, LTs are integer multiples of 30 min, ranging from −30 min to 120 min. All LTs are classified into four types: −30 min, 0, 30 min, and ≥60 min (their respective percentages in each diurnal/monthly/landscape category are represented by shaded bars, from dark to light gray). Variations in mean LT (the mean value of all LTs in each category) are shown in purple.
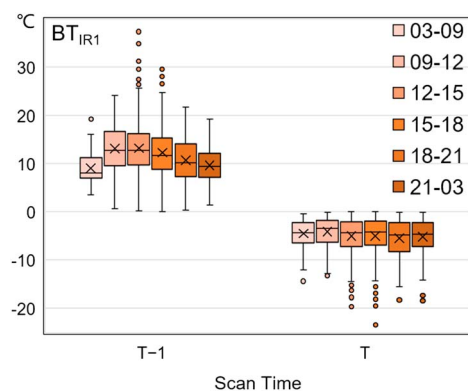

Figure 11. Box-and-whisker plot of BT_{IR1} (as a function of scan time) derived from FY-2E, for all 1,630 satellite-derived CI signals within the diurnal framework. The plotting style for the box-and-whisker plot is given in Figure 6c.

(Figure 12b). However, more negative LTs and smaller positive LTs are present in CEC in midsummer (Figures 12c and 12d). During the EASM period, more warm and moist air from the tropical and subtropical oceans prevails over CEC from May to August, providing more precipitable water (Figure 8), especially more liquid water content, which is more favorable for convective storms to begin with a warm-rain process (Jewett & Mecikalski, 2013). This partly accounts for the monthly increase in the percentage of −30 min and zero LTs and thus the monthly decrease in mean LT (Figure 10b).

In addition to the warm-rain process, the intensifying cloud development as the summer progresses should also be factored in the analysis of the intraseasonal variation of LT. The BT_{IR1} field can be used to assess cloud top height. Lower BT_{IR1} generally indicates a higher cloud top. With a mean and median greater than 10°C, BT_{IR1} at $T − 1$ (Figure 13a) suggests that the signal locations are mostly warm-cloud covered or cloudless before signal formation. A slight increase in BT_{IR1} from May to August (a total increment of about 1°C in both mean and median) is likely associated with the intraseasonal terrestrial warming. However, BT_{IR1} at T shows a slightly decreasing trend (Figure 13a) when satellite-derived CI signals form and cloud tops reach subfreezing level. Such a decreasing trend becomes significant at $T + 1$ when high clouds develop (Figure 13a), indicating that the cumulus clouds undergoing CI generally develop to a higher altitude as the summer progresses. Cloud growth rate can be inferred from the BT_{IR1} time trend, in which a more negative value implies more rapid cloud development. The BT_{IR1} time trend fields of different scan intervals consistently exhibit a more negative monthly trend (Figure 13b), suggesting faster cloud development as the summer progresses, which is likely due to increasing moisture (Figure 8) and background instability (Figure 9). A larger growth rate makes cumulus cloud achieve altitude faster, enabling the onset of significant rainfall (35 dBZ radar echoes in this study) and leading to a smaller mean LT (Figure 10b).

4.3. Landscape Variation

Satellite-derived CI signals over distinct landscapes were collected to investigate how LTs respond to different configurations of topography in CEC. Five landscapes were selected according to elevation range: coastal sea (<0 m), plain (0–200 m), hill (200–500 m), mountain (500–1000 m), and plateau (>1000 m). The results show that higher-elevation landscapes (Figure 6c) tend to have longer LTs with a mean value increasing from 1 min over coastal sea to 19 min over plateau (Figure 10c). As a typical monsoon climate region, CEC has a tropical environment during the EASM period, which contributes to the production of more warm-rain processes in early stages of new cumulus clouds (Walker et al., 2012). This leads to shorter satellite-derived LTs for the detection of ≥35 dBZ radar echoes in CEC compared with other midlatitude counterparts. For example, Walker et al. (2012) found a mean LT of between 24 and 33 min over different regions across the continental United States, versus a mean LT of between 1 and 19 min over various landscapes in CEC (Figure 10c) in our study.

The coastal sea and plain have shorter mean LTs (Figure 10c) of the five landscapes. More negative or zero LTs over the coastal sea and plain than over other landscapes (Figure 10c) indicate that these two
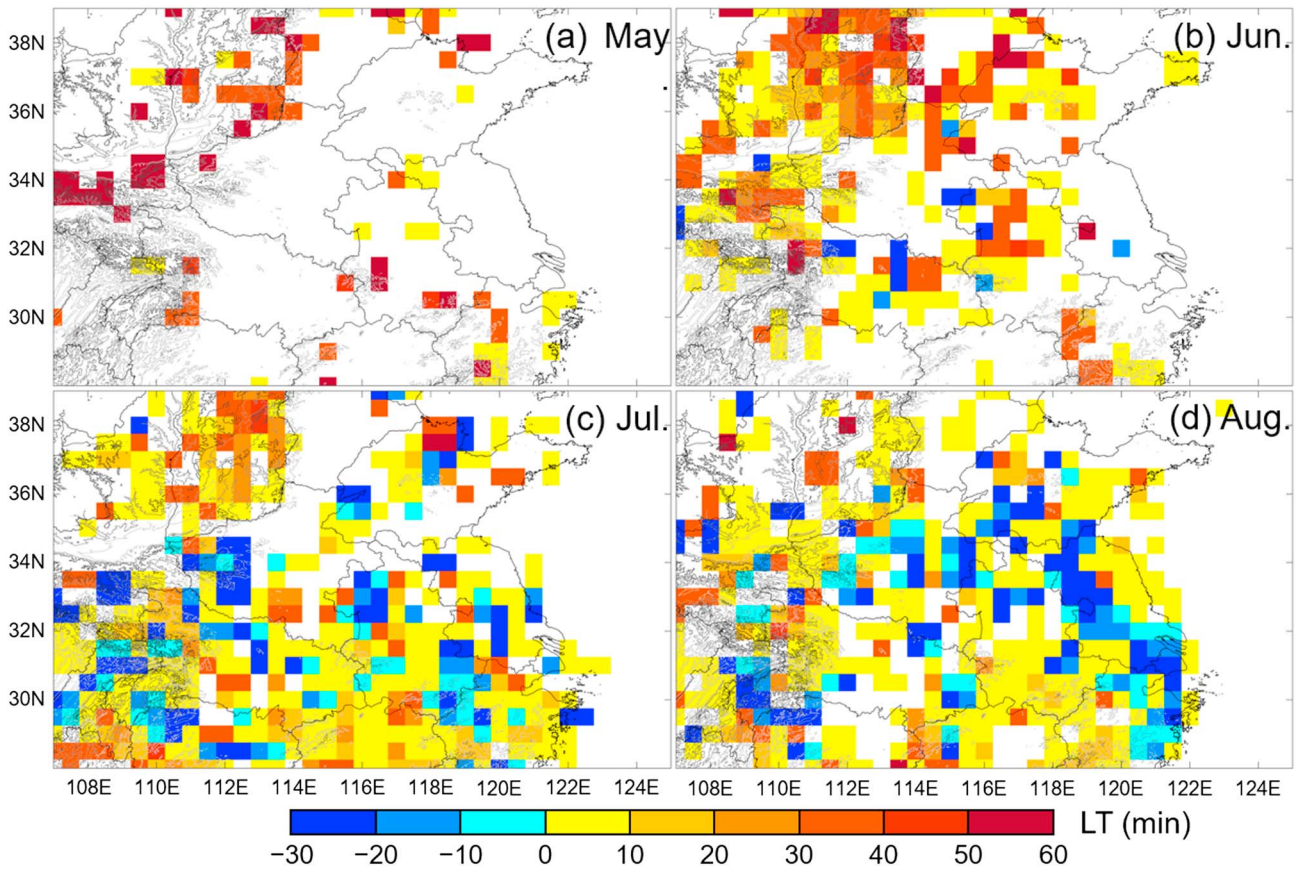
Figure 12. The 0.5° × 0.5° mosaic plots of LT (the lead time of signal formation time before the CI time) in (a) May, (b) June, (c) July, and (d) August over central eastern China. For each 0.5° × 0.5° grid, the LT was calculated as the mean LT of all satellite-derived CI signals within or across this grid to ensure the statistical significance. The topographic elevations of 500, 1,000, and 1,500 m are represented by gray (from light to dark) contour lines.

landscapes tend to have more warm-rain processes due to more precipitable water transported by the EASM into these two landscapes (Figure 8).

The increase in mean LT from hill to mountain and the plateau can be interpreted in terms of different cloud development over these landscapes. At $T-1$, CI-related clouds are low or have not yet appeared over signal locations, as indicated by high mean BT_{IR1} (Figure 14a) ranging from 11 to 12°C. As the
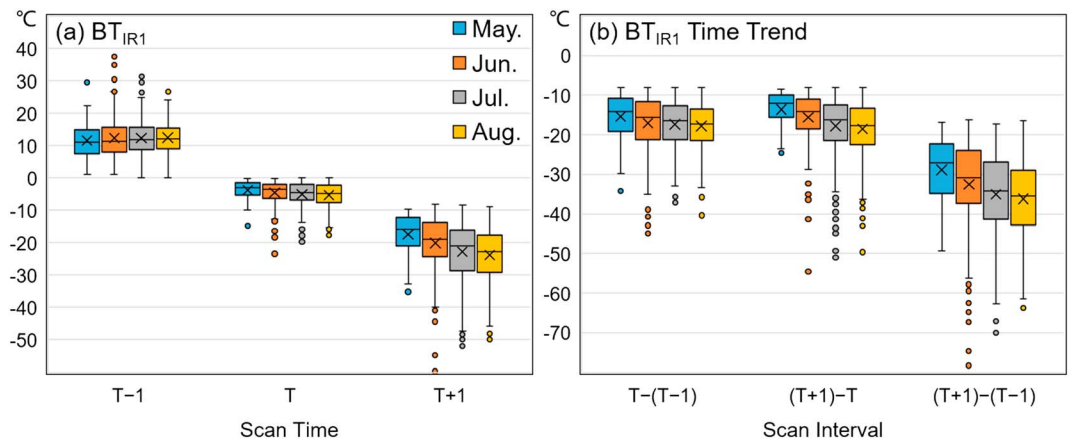

Figure 13. Box-and-whisker plots of (a) BT_{IR1} field (as a function of scan time) and (b) its time trend (as a function of scan interval) derived from FY-2E, for all 1,630 satellite-derived CI signals within the monthly framework. The plotting style for box-and-whisker plots is given in Figure 6c.
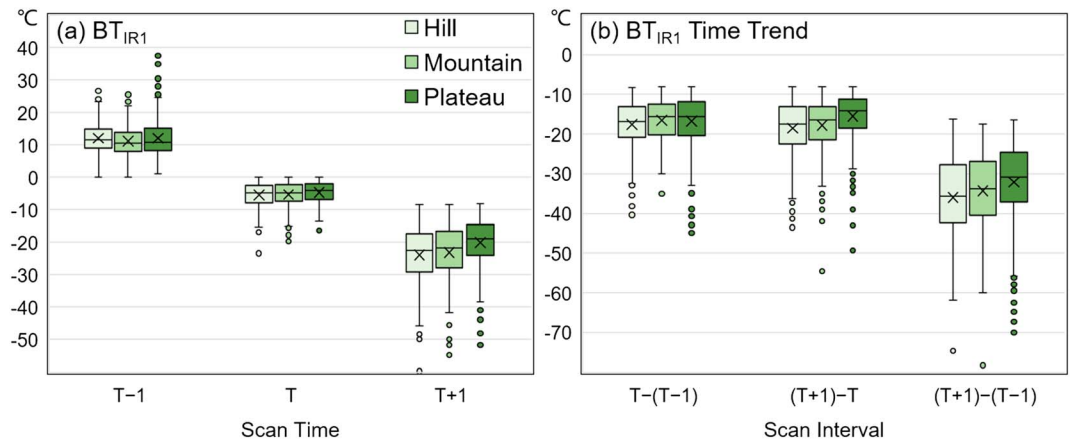
Figure 14. As in Figure 13 but within the landscape (hill, mountain, and plateau) framework.

clouds keep growing until signal formation, the cloud tops extend to a slightly higher altitude (lower BT_{IR1} at T in Figure 14a) over hill than over other landscapes. Such altitude differences become evident at $T + 1$, characterized by mean (median) BT_{IR1} ranging from -24 (-23)°C (hill) to -20 (-19)°C (plateau). The BT_{IR1} time trends between different scan times in different landscapes (Figure 14b) suggest that the cloud growth rate is decreasing from over hill, to mountain, and the plateau, resulting in increasing LTs from hill to plateau (Figure 10c).

In summary, the slower cloud growth from hill to plateau, together with the dominant warm-rain process in coastal sea and plain areas, accounts for the increase in mean LT as the landscape elevation increases (Figure 10c). The landscape variation of LT is consistent with the intraseasonal variation of LT. The longer LTs generally occur in northwest highlands during early summer, while the smaller LTs generally occur in southeast lowlands during midsummer (Figure 12).

5. Summary

Based on the Chinese operational geostationary satellite FY-2E and radar mosaics, this study investigated the spatial and temporal variations of satellite-derived signals of isolated CI processes in central eastern China (CEC) during the warm season of 2010. These satellite-derived CI signals were identified using a semiauto-mated method designed in this work. The brightness temperature (BT) data from the FY-2E IR1 channel on a grid of $0.05° \times 0.05°$ at 30 min intervals were utilized to produce candidate signals involving grid(s) with a cooling rate of no less than 8°C per 30 min. The satellite-derived candidate signals were then validated with radar-based isolated CI events to produce the final 1,630 satellite-derived CI signals for statistical analyses. The probability of detection (POD) of satellite-derived CI signals over radar-detected isolated CI events is 50.3%, which is comparable with those in the United States.

The results show that the satellite-derived CI signals have a major peak in the early afternoon when solar heating is strongest. The monthly mean frequency of satellite-derived CI signals increases from 2 per day in May to 39 per day in August. Most of the satellite-derived CI signals occur over the areas with remarkable landscape inhomogeneity in CEC. A shift in the high signal frequency areas from northwest CEC (dry, mainly highlands) in early summer to southeast CEC (humid, mainly lowlands) in midsummer was observed, likely associated with the northward migration of the East Asia summer monsoon into the summer.

The lead times (LTs) of satellite-derived CI signals relative to radar-derived isolated CI signatures demonstrate apparent diurnal, monthly, and landscape variabilities. The satellite-derived CI signals have overall longer LTs in the late morning and afternoon when the solar heating is strongest. During the night and early morning, the distinction between cloud top signatures and background terrestrial radiation becomes less apparent in IR1 imagery, resulting in delayed identification of signals and thus short LTs. During monsoon period, more tropical environments in CEC contribute to the occurrence of more warm-rain processes in early stages of cumulus clouds before satellite-derived signal formation time, consequently resulting in more negative LTs. The mean LT declines from May to August, likely because of a larger cloud growth rate and more

warm-rain processes into the summer. The mean LT increases consistently from the coastal sea, to the plain, hill, and mountain, up to the plateau in CEC. It is likely that more warm-rain processes over the coastal sea and plain coupled with the slower cloud growth from hill to mountain and the plateau account for the increasing LTs over more elevated landscapes in CEC. These results may become a helpful reference for CI nowcasting in China as well as places with similar climate regimes around the globe.

In the near future, we will expand our current work using data from new generation geostationary satellites, such as Himawari-8 and the newly launched FY-4 (FY-2 successor), which are equipped with sensors that can provide more rapid scans, finer details, and more spectral channels (Bessho et al., 2016; Yang et al., 2017).

References

Ai, Y., Li, W., Meng, Z., & Li, J. (2016). Life cycle characteristics of MCSs in middle East China tracked by geostationary satellite and precipitation estimates. *Monthly Weather Review*, *144*(7), 2517–2530. https://doi.org/10.1175/MWR-D-15-0197.1

Amante, C., & Eakins, B. (2009). ETOPO1 1 arc-minute global relief model: Procedures, data sources and analysis, NOAA Tech. Memo. NESDIS NGDC-24, NOAA NGDC. https://doi.org/10.7289/V5C8276M

American Meteorological Society (2017). Warm rain, glossary of meteorology. Retrieved from: http://glossary.ametsoc.org/wiki/Warm_rain

Banta, R. M., & Barker Schaaf, C. (1987). Thunderstorm genesis zones in the Colorado Rocky Mountains as determined by traceback of geosynchronous satellite images. *Monthly Weather Review*, *115*(2), 463–476. https://doi.org/10.1175/1520-0493(1987)115%3C0463:TGZITC%3E2.0.CO;2

Barker Schaaf, C., Wurman, J., & Banta, R. M. (1988). Thunderstorm producing terrain features. *Bulletin of the American Meteorological Society*, *69*(3), 272–277. https://doi.org/10.1175/1520-0477(1988)0690272:TPTF.2.0.CO;2

Bessho, K., Date, K., Hayashi, M., Ikeda, A., Imai, T., Inoue, H., … Yoshida, R. (2016). An introduction to Himawari-8/9—Japan's new-generation geostationary meteorological satellites. *Journal of the Meteorological Society of Japan*, *94*(2), 151–183. https://doi.org/10.2151/%20jmsj.2016-009

Chen, B., & Liu, C. (2016). Warm organized rain system over the tropical Pacific. *Journal of Climate*, *29*(9), 3403–3422. https://doi.org/10.1175/JCLI-D-15-0177.1

Fovell, R. G. (2005). Convective initiation ahead of the sea-breeze front. *Monthly Weather Review*, *133*(1), 264–278. https://doi.org/10.1175/MWR-2852.1

Gambill, L. D., & Mecikalski, J. R. (2011). A satellite-based summer convective cloud frequency analysis over the southeastern United States. *Journal of Applied Meteorology and Climatology*, *50*(8), 1756–1769. https://doi.org/10.1175/2010JAMC2559.1

Harris, R. J., Mecikalski, J. R., MacKenzie, W. M. Jr., Durkee, P. A., & Nielsen, K. E. (2010). The definition of GOES infrared lightning initiation interest fields. *Journal of Applied Meteorology and Climatology*, *49*(12), 2527–2543. https://doi.org/10.1175/2010JAMC2575.1

Houze, R. A. Jr. (2012). Orographic effects on precipitating clouds. *Reviews of Geophysics*, *50*, RG1001. https://doi.org/10.1029/2011RG000365

Houze, R. A. Jr., Rasmussen, K. L., Zuluaga, M. D., & Brodzik, S. R. (2015). The variable nature of convection in the tropics and subtropics: A legacy of 16 years of the Tropical Rainfall Measuring Mission satellite. *Reviews of Geophysics*, *53*(3), 994–1021. https://doi.org/10.1002/2015RG000488

Houze, R. A. Jr., Wilton, D. C., & Smull, B. F. (2007). Monsoon convection in the Himalayan region as seen by the TRMM precipitation radar. *Quarterly Journal of the Royal Meteorological Society*, *133*, 1389–1411. https://doi.org/10.1002/qj.106

Jewett, C. P., & Mecikalski, J. R. (2013). Adjusting thresholds of satellite-based convective initiation interest fields based on the cloud environment. *Journal of Geophysical Research: Atmospheres*, *118*(22), 12,649–12,660. https://doi.org/10.1002/2013JD019700

Laird, N. F., Kristovich, D. A. R., Liang, X., Arritt, R. W., & Labas, K. (2001). Lake Michigan lake breezes: Climatology, local forcing, and synoptic environment. *Journal of Applied Meteorology*, *40*(3), 409–424. https://doi.org/10.1175/1520-0450(2001)0400409:LMLBCL.2.0.CO;2

Lima, M. A., & Wilson, J. W. (2008). Convective storm initiation in a moist tropical environment. *Monthly Weather Review*, *136*(6), 1847–1864. https://doi.org/10.1175/2007MWR2279.1

Liu, C., & Zipser, E. (2009). "Warm rain" in the tropics: Seasonal and regional distributions based on 9 yr of TRMM data. *Journal of Climate*, *22*(3), 767–779. https://doi.org/10.1175/2008JCLI2641.1

Liu, C., Zipser, E. J., Cecil, D. J., Nesbitt, S. W., & Sherwood, S. (2008). A cloud and precipitation feature database from 9 years of TRMM observations. *Journal of Applied Meteorology and Climatology*, *47*(10), 2712–2728. https://doi.org/10.1175/2008JAMC1890.1

Luo, Y., Wang, H., Zhang, R., Qian, W., & Luo, Z. (2013). Comparison of rainfall characteristics and convective properties of monsoon precipitation systems over South China and the Yangtze and Huai River basin. *Journal of Climate*, *26*(1), 110–132. https://doi.org/10.1175/JCLI-D-12-00100.1

Madaus, L., & Hakim, G. (2016). Observable surface anomalies preceding simulated isolated convective initiation. *Monthly Weather Review*, *144*(6), 2265–2284. https://doi.org/10.1175/MWR-D-15-0332.1

Markowski, P., & Richardson, Y. (2010). *Mesoscale meteorology in midlatitudes.* John Wiley. https://doi.org/10.1002/9780470682104

Mecikalski, J. R., & Bedka, K. M. (2006). Forecasting convective initiation by monitoring the evolution of moving cumulus in daytime GOES imagery. *Monthly Weather Review*, *134*(1), 49–78. https://doi.org/10.1175/MWR3062.1

Mecikalski, J. R., Bedka, K. M., Paech, S. J., & Litten, L. A. (2008). A statistical evaluation of GOES cloud-top properties for predicting convective initiation. *Monthly Weather Review*, *136*(12), 4899–4914. https://doi.org/10.1175/%202008MWR2352.1

Mecikalski, J. R., Li, X., Carey, L. D., McCaul, E. W. Jr., & Coleman, T. A. (2013). Regional comparison of GOES cloud-top properties and radar characteristics in advance of first-flash lightning initiation. *Monthly Weather Review*, *141*(1), 55–74. https://doi.org/10.1175/MWR-D-12-00120.1

Mecikalski, J. R., Mackenzie, W. M., Koenig, M., & Muller, S. (2010a). Cloud-top properties of growing cumulus prior to convective initiation as measured by Meteosat second generation. Part I: Infrared fields. *Journal of Applied Meteorology and Climatology*, *49*(3), 521–534. https://doi.org/10.1175/2009JAMC2344.1

Mecikalski, J. R., Mackenzie, W. M., Koenig, M., & Muller, S. (2010b). Cloud-top properties of growing cumulus prior to convective initiation as measured by Meteosat second generation. Part II: Use of visible reflectance. *Journal of Applied Meteorology and Climatology*, *49*(12), 2544–2558. https://doi.org/10.1175/2010JAMC2480.1

Mecikalski, J. R., Williams, J. K., Jewett, C. P., Ahijevych, D., Leroy, A., & Walker, J. (2015). Probabilistic 0–1-h convective initiation nowcasts that combine geostationary satellite observations with numerical weather prediction model data. *Journal of Applied Meteorology and Climatology*, *54*(5), 1039–1059. https://doi.org/10.1175/JAMC-D-14-0129.1

Medina, S., Houze, R. A. Jr., Kumar, A., & Niyogi, D. (2010). Summer monsoon convection in the Himalayan region: Terrain and land cover effects. *Quarterly Journal of the Royal Meteorological Society*, *136*, 593–616. https://doi.org/10.1002/qj.601

Meng, Z., Yan, D., & Zhang, Y. (2013). General features of squall lines in east China. *Monthly Weather Review*, *141*(5), 1629–1647. https://doi.org/10.1175/%20MWR-D-12-00208.1

Purdom, J. F. W. (1976). Some uses of high resolution GOES imagery in the mesoscale forecasting of convection and its behavior. *Monthly Weather Review*, *104*(12), 1474–1483. https://doi.org/10.1175/1520-0493(1976)104%3C1474:SUOHRG%3E2.0.CO;2

Qian, T., Epifanio, C. C., & Zhang, F. (2012). Topographic effects on the tropical land and sea breeze. *Journal of the Atmospheric Sciences*, *69*(1), 130–149. https://doi.org/10.1175/JAS-D-11-011.1

Qin, F., & Fu, Y. (2016). TRMM-observed summer warm rain over the tropical and subtropical Pacific Ocean: Characteristics and regional differences. *Journal of Meteorological Research*, *30*(3), 371–385. https://doi.org/10.1007/s13351-016-5151-x

Rasmussen, K. L., & Houze, R. A. Jr. (2011). Orogenic convection in subtropical South America as seen by the TRMM satellite. *Monthly Weather Review*, *139*(8), 2399–2420. https://doi.org/10.1175/MWR-D-10-05006.1

Rasmussen, K. L., & Houze, R. A. Jr. (2016). Convective initiation near the Andes in subtropical South America. *Monthly Weather Review*, *144*(6), 2351–2374. https://doi.org/10.1175/MWR-D-15-0058.1

Roberts, R. D., & Rutledge, S. (2003). Nowcasting storm initiation and growth using GOES-8 and WSR-88D data. *Weather and Forecasting*, *18*(4), 562–584. https://doi.org/10.1175/1520-0434(2003)018,0562:%20NSIAGU.2.0.CO;2

Schumacher, C., & Houze, R. A. Jr. (2003). The TRMM precipitation radar's view of shallow isolated rain. *Journal of Applied Meteorology*, *42*(10), 1519–1524. https://doi.org/10.1175/1520-0450(2003)042,1519:%20TTPRVO.2.0.CO;2

Senf, F., & Deneke, H. (2017). Satellite-based characterization of convective growth and glaciation and its relationship to precipitation formation over central Europe. *Journal of Applied Meteorology and Climatology*, *56*(7), 1827–1845. https://doi.org/10.1175/JAMC-D-16-0293.1

Sieglaff, J. M., Cronce, L. M., Feltz, W. F., Bedka, K. M., Pavolonis, M. J., & Heidinger, A. K. (2011). Nowcasting convective storm initiation using satellite-based box-averaged cloud-top cooling and cloud-type trends. *Journal of Applied Meteorology and Climatology*, *50*(1), 110–126. https://doi.org/10.1175/2010JAMC2496.1

Siewert, C. W., Koenig, M., & Mecikalski, J. R. (2010). Application of Meteosat second generation data towards improving the nowcasting of convective initiation. *Meteorological Applications*, *17*, 442–451. https://doi.org/10.1002/met.176

Small, C. (2004). Global population distribution and urban land use in geophysical parameter space. *Earth Interactions*, *8*(8), 1–18. https://doi.org/10.1175/1087-3562(2004)008%3C0001:GPDAUL%3E2.0.CO;2

Soderholm, B., Ronalds, B., & Kirshbaum, D. J. (2014). The evolution of convective storms initiated by an isolated mountain ridge. *Monthly Weather Review*, *142*(4), 1430–1451. https://doi.org/10.1175/%20MWR-D-13-00280.1

Umek, L., & Gohm, A. (2016). Lake and orographic effects on a snowstorm at Lake Constance. *Monthly Weather Review*, *144*(12), 4687–4707. https://doi.org/10.1175/MWR-D-16-0032.1

Walker, J. R., MacKenzie, W. M., Mecikalski, J. R., & Jewett, C. P. (2012). An enhanced geostationary satellite–based convective initiation algorithm for 0–2-h nowcasting with object tracking. *Journal of Applied Meteorology and Climatology*, *51*(11), 1931–1949. https://doi.org/10.1175/JAMC-D-11-0246.1

Weaver, C. P., & Avissar, R. (2001). Atmospheric disturbances caused by human modification of the landscape. *Bulletin of the American Meteorological Society*, *82*(2), 269–281. https://doi.org/10.1175/1520-0477(2001)0820269:%20ADCBHM.2.3.CO;2

Weaver, J. F., & Nelson, S. P. (1982). Multiscale aspects of thunderstorm gust fronts and their effects on subsequent storm development. *Monthly Weather Review*, *110*(7), 707–718. https://doi.org/10.1175/%201520-0493(1982)1100707:MAOTGF.2.0.CO;2

Weckwerth, T. M., & Parsons, D. B. (2006). A review of convection initiation and motivation for IHOP_2002. *Monthly Weather Review*, *134*(1), 5–22. https://doi.org/10.1175/MWR3067.1

Westcott, N. (1994). Merging of convective clouds: Cloud initiation, bridging, and subsequent growth. *Monthly Weather Review*, *122*(5), 780–790. https://doi.org/10.1175/1520-0493(1994)122,0780:MOCCCI.2.0.CO;2

Wu, Q., Wang, H.-Q., Zhuang, Y.-Z., Lin, Y.-J., Zhang, Y., & Ding, S.-S. (2016). Correlations of multispectral infrared indicators and applications in the analysis of developing convective clouds. *Journal of Applied Meteorology and Climatology*, *55*(4), 945–960. https://doi.org/10.1175/JAMC-D-15-0081.1

Wulfmeyer, V., Behrendt, A., Bauer, H.-S., Kottmeier, C., Corsmeier, U., Blyth, A., … Simmer, C. (2008). The convective and orographically induced precipitation study: A research and development project of the World Weather Research Program for improving quantitative precipitation forecasting in low-mountain regions. *Bulletin of the American Meteorological Society*, *89*(10), 1477–1486. https://doi.org/10.1175/2008BAMS2367.1

Xu, W. (2013). Precipitation and convective characteristics of summer deep convection over East Asia observed by TRMM. *Monthly Weather Review*, *141*(5), 1577–1592. https://doi.org/10.1175/MWR-D-12-00177.1

Yang, G.-Y., & Slingo, J. (2001). The diurnal cycle in the tropics. *Monthly Weather Review*, *129*(4), 784–801. https://doi.org/10.1175/1520-0493(2001)129,0784:%20TDCITT.2.0.CO;2

Yang, J., Zhang, Z., Wei, C., Lu, F., & Guo, Q. (2017). Introducing the new generation of Chinese geostationary weather satellites, Fengyun-4. *Bulletin of the American Meteorological Society*, *98*(8), 1637–1658. https://doi.org/10.1175/BAMS-D-16-0065.1

Yang, X., Fei, J., Huang, X., Cheng, X., Carvalho, L. M. V., & He, H. (2015). Characteristics of mesoscale convective systems over China and its vicinity using geostationary satellite FY2. *Journal of Climate*, *28*(12), 4890–4907. https://doi.org/10.1175/JCLI-D-14-00491.1

Zheng, L., Sun, J., Zhang, X., & Liu, C. (2013). Organizational modes of mesoscale convective systems over central east China. *Weather and Forecasting*, *28*(5), 1081–1098. https://doi.org/10.1175/WAF-D-12-00088.1

Ziegler, C. L. (2014). Deep convection initiation: State of the science, limits of understanding, and future directions, paper presented at 94th American Meteorological Society Annual Meeting, Amer. Meteor. Soc., Atlanta, GA.

Zipser, E. J., Liu, C., Cecil, D. J., Nesbitt, S. W., & Yorty, D. P. (2006). Where are the most intense thunderstorms on Earth? *Bulletin of the American Meteorological Society*, *87*(8), 1057–1071. https://doi.org/10.1175/BAMS-87-8-1057